Evidence for a large Rashba splitting in $PtPb_4$ from angle-resolved photoemission spectroscopy

Kyungchan Lee,[1,2] Daixiang Mou,[1,2] Na Hyun Jo,[1,2] Yun Wu,[1,2] Benjamin Schrunk,[1,2] John M. Wilde,[1,2] Andreas Kreyssig,[1,2] Amelia Estry,[1] Sergey L. Bud'ko,[1,2] Manh Cuong Nguyen,[1,2] Lin-Lin Wang,[1,2] Cai-Zhuang Wang,[1,2] Kai-Ming Ho,[1,2] Paul C. Canfield,[1,2,*] and Adam Kaminski[1,2,†]

[1]*Ames Laboratory, U.S. Department of Energy, Ames, Iowa 50011, USA*

[2]*Department of Physics and Astronomy, Iowa State University, Ames, Iowa 50011, USA*

(Received 1 September 2020; revised 6 January 2021; accepted 27 January 2021; published 18 February 2021)

We studied the electronic structure of $PtPb_4$ using laser angle-resolved photoemission spectroscopy (ARPES) and density functional theory (DFT) calculations. This material is closely related to $PtSn_4$, which exhibits exotic topological properties such as Dirac node arcs. The Fermi surface (FS) of $PtPb_4$ consists of two electron pockets at the center of the Brillouin zone (BZ) and several hole pockets around the zone boundaries. Our ARPES data reveal significant Rashba splitting at the Γ point, in agreement with DFT calculations. The presence of Rashba splitting may render this material of potential interest for spintronic applications.

DOI: 10.1103/PhysRevB.103.085125

I. INTRODUCTION

Recently, the search for new topological materials has resulted in a number of discoveries of very interesting materials and has become a popular trend in condensed-matter physics. Unique topological states such as spin-momentum locking [1], conductive surface states [2], backscattering suppression [3], the Fermi arc [4], and surface states protected by time-reversal symmetry [2,5] offer the promise of a wide range of applications and significant advancement of computing technologies [6–11]. The ability to generate spin currents in topological materials is very important for spintronic applications [11]. The search for novel topological materials often starts with theoretical investigations such as density functional theory(DFT) calculations later confirmed by experimental studies [4,12–15].

Recent measurements of the band structure in $PtSn_4$ revealed Dirac node arcs which are Dirac-like dispersions extending along a one-dimensional line instead of having cylindrical symmetry [16]. $PtSn_4$ is composed of Sn-Pt-Sn layers along the *b* axis with orthorhombic structure [17]. This is a rare example of the discovery of a topological material done by experiment rather than theory.

Building on our success with $PtSn_4$, we undertook an investigation of related materials to understand the origin of the Dirac node arc. We examined transport properties and band structures of $PdSn_4$, which belongs to the same structural family as $PtSn_4$ [18]. In the case of $PdSn_4$, the Dirac node arc disappears, but the single Dirac cone still persists upon replacing Pt with Pd. This might indicate that the Dirac node arc could be sensitive to spin-orbit coupling (SOC).

To better understand the properties of $PtSn_4$ and structurally related ultraheavy compounds with large SOC, we studied the electronic structure of $PtPb_4$. Interestingly, this material is a superconductor with T_C of 2.4 K [19]. In addition, it is an efficient electrocatalyst used in hydrogen fuel cells, which are important for renewable energy [6,20]. $PtPb_4$ crystallizes in a tetragonal structure that is qualitatively very similar to the structure of $PtSn_4$. $PtPb_4$ is composed of Pb-Pt-Pb slabs that are similar to the Sn-Pt-Sn slabs in $PtSn_4$. $PtPb_4$ has lattice constants $a = b = 6.667$ Å and $c = 5.978$ Å [21] and is predicted to be a strong topological insulator. Although $PtSn_4$ and structurally related systems have been studied intensively, $PtPb_4$ has eluded experimental studies of its electronic properties. Here, we report the electronic structure of $PtPb_4$ by using ultrahigh-resolution angle-resolved photoemission spectroscopy (ARPES) and DFT calculations. We found more than two electron pockets at the center of the Brillouin zone (BZ) and several hole pockets around zone boundaries in each direction. Intriguingly, our ARPES data show twofold symmetry even though the crystal structure is tetragonal. X-ray data and DFT calculations show that this symmetry is due to a modified stacking of the Pb-Pt-Pb layers of the material.

Our measurements reveal large Rashba splitting (RS) at a binding energy of 1.3 eV. RS is a breaking of spin degeneracy as a result of SOC and inversion symmetry breaking. Although SOC appears in various systems, it is stronger in materials with high-*Z* elements due to the relatively larger spin-orbit parameter. Since RS is a spin-polarized surface state, it is expected to be useful in the generation of spin currents and manipulation of spin polarization by the electric field for spintronic devices [22]. Despite decades of research, the operation of spintronic devices is very limited to low temperatures. Previous research demonstrates that a spin-injected field effect transistor controlled by gate voltage operates at 1.8 K [23] and the spin Hall effect transistor works at 4 K [24]. One of the major turning points in spintronic devices is using the spin-polarized state of large RS. It was initially discussed for a wurtzite structure [25] and intensively studied

*canfield@ameslab.gov
†adamkam@ameslab.gov

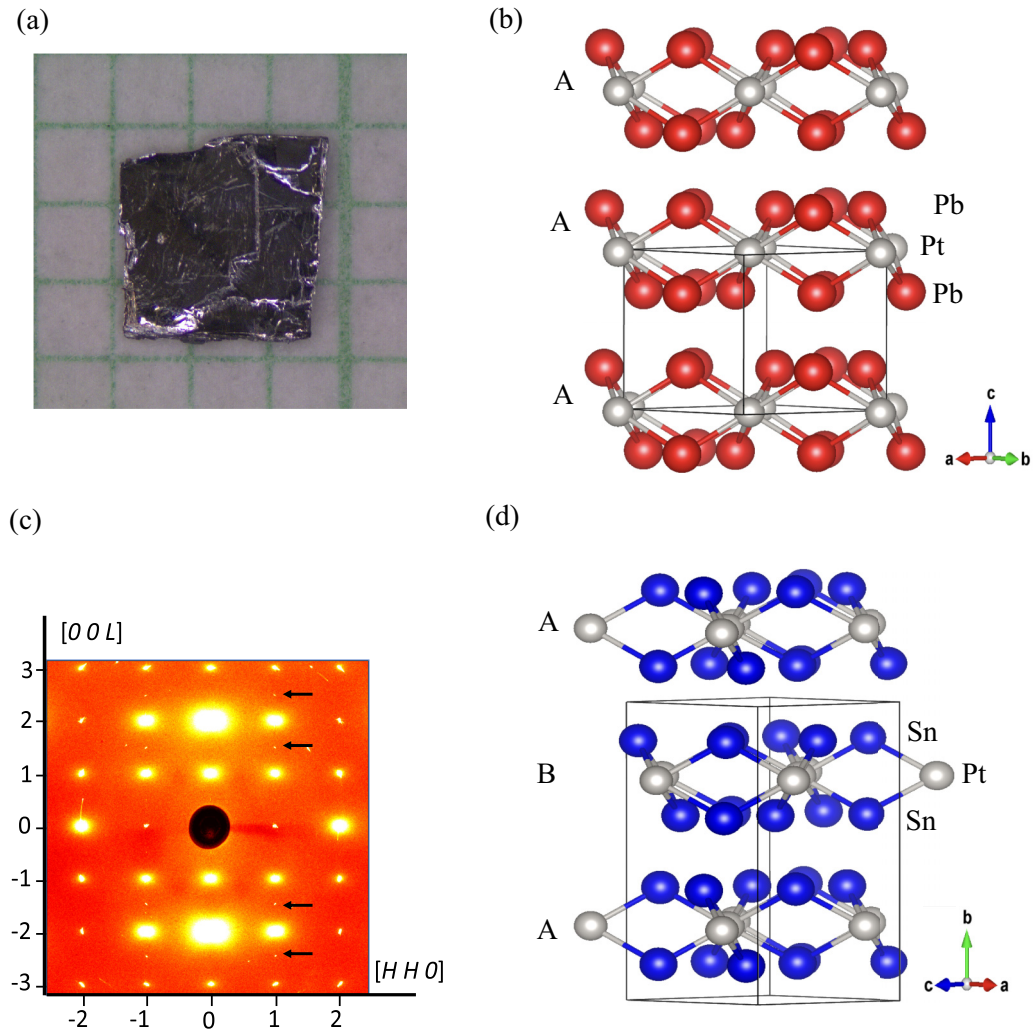

FIG. 1. Single crystal of $PtPb_4$, x-ray scattering data for $PtPb_4$, and crystal structures of $PtPb_4$ and $PtSn_4$. (a) Photograph of the $PtPb_4$ single crystal on a millimeter grid, (b) the tP10 structure of $PtPb_4$ with the space group $P4/nbm$, (c) the high-energy x-ray diffraction pattern of the (HHL) plane, and (d) the oS20 structure of $PtSn_4$ with space group $Ccce$.

in various metals [26–28], some alloys [29,30], thin films [11,31,32], and semiconductors [33–38] which show giant Rashba splitting. Semiconductors typically show small RS, which is not suitable for room temperature spintronic devices. On the other hand, metals show relatively large RS, but the spin polarization cannot be controlled by an external electric field. Our ARPES data and DFT calculations show that the RS in $PtPb_4$ is comparable to those of metal surface states. New generation spintronics devices working at room temperature need large splitting between spin-polarized bands and demand tunability of the chemical potential. Consequently, the spin-polarized surface state in $PtPb_4$ gives us a chance to control the spin without applying magnetic fields at room temperature, paving the way for developing more efficient spintronics devices.

II. METHODS

Single crystals of $PtPb_4$ were grown out of Pb-rich binary melts [39]. We put three different initial stoichiometries of $Pt_{13}Pb_{87}$, $Pt_{11}Pb_{89}$, and Pt_9Pb_{91} into fritted alumina crucibles Canfield crucible set [40] and then sealed it into amorphous silica tubes under partial Ar atmosphere. The ampoules were heated up to 600 °C, held there for 5 h, rapidly cooled to 375 °C, then slowly cooled down to 310 °C over more than 100 h, and then finally decanted using a centrifuge. The single-crystalline samples have a clear platelike shape with a mirrored surface. Figure 1(a) shows a photograph of a single crystal of $PtPb_4$ on a millimeter scale. Typical crystals have dimensions of $3\times3\times0.5\,mm^3$. The crystallographic c axis is perpendicular to the platelike plane.

High-energy x-ray diffraction measurements were performed at station 6-ID-D at the Advanced Photon Source, Argonne National Laboratory. Measurements were made using 100-keV x rays, with the incident beam direction normal to the (HHL) reciprocal-lattice planes. Diffraction patterns were recorded using a MAR345 area detector. Unlike laboratory sources, high-energy x rays ensure that the bulk of the sample is probed. By rocking the sample through small angular ranges about the axes perpendicular to the incident beam, we obtain an image of the

reciprocal-lattice planes normal to the incident beam direction [41].

The DFT [42] calculations are performed using the Vienna Ab initio Simulation Package (VASP) [43] with the projector augmented-wave pseudopotential method [44,45] within the generalized-gradient approximation (GGA) [46]. The energy cutoff is 300 eV, and the Monkhorst-Pack scheme [47] is used for Brillouin zone sampling with a high-quality **k**-point mesh of $8\times8\times8$ for tetragonal $PtPb_4$ and $8\times4\times8$ for orthorhombic $PtPb_4$ structures. All structures are fully relaxed until the forces acting on each atom are smaller than 0.01 eV/Å and all stress tensor elements are smaller than 1 kbar (0.1 GPa). Since both Pt and Pb are heavy elements, the relativistic effect is not negligible and is taken into account via SOC calculations. The van der Waals (vdW) interaction is also taken into account by the DFT-D3 method [48,49]. The surface formation energy is calculated by a slab model. The slab model consists six $PtPb_4$ layers with two identical surfaces [(001) for the tetragonal and (010) for the orthorhombic structures] and a vacuum region of more than 20 Å in the direction perpendicular to the surfaces to avoid interaction between the slab and its images due to periodic boundary conditions. A supercell of 2×2 in the lateral directions is used and contains 60 atoms. The two center layers are kept fixed at bulk atomic positions, while atomic positions of the two outermost layers for each surface are relaxed. SOC and vdW interactions are included in the surface formation energy calculation.

ARPES measurements were carried out using a laboratory-based tunable VUV laser. The ARPES system consists of a Scienta R8000 electron analyzer, picosecond Ti:sapphire oscillator, and fourth-harmonic generator [50]. All data were collected with 6.7 eV of photon energy. Angular resolution was set at 0.1° and 1° along and perpendicular to the direction of the analyzer slit, respectively, and the energy resolution was set at 2 meV. The size of the photon beam on the sample was ~30 μm. Samples were cleaved *in situ* at a base pressure lower than 1×10^{-10} Torr at 40 K and kept at the cleaving temperature throughout the measurement.

III. RESULTS AND DISCUSSION

The previously reported crystal structure of $PtPb_4$ consists of stacked Pb-Pt-Pb layers along the c axis as shown in Fig. 1(b). The gray spheres represent Pt atoms, and red spheres are Pb atoms. High-energy x-ray diffraction data were taken on a single-crystal sample of $PtPb_4$ as seen in Fig. 1(c) to search for any structural anomalies such as orthorhombicity. No peak broadening or splitting was observed, but additional peaks are clearly observed at half L positions of $(1, 1, L)$ in Fig. 1(c), which are marked by black arrows. These peaks are forbidden for the reported space group of $PtPb_4$, and the resulting reflection conditions are not consistent with any tetragonal space group. However, several orthorhombic crystal structures like $PtSn_4$ would be consistent with the observed doubling of the unit cell in the c direction indicated by the additional half-integer Bragg peaks and the observed reflection conditions. Figure 1(d) shows the most closely related oS20 of the $PtSn_4$-type structure by simply changing the stacking order. Gray balls represent Pt atoms, and blue ones are Sn atoms.

TABLE I. Relative formation energy (in meV/atom) of tetragonal $PtPb_4$ to orthorhombic $PtPb_4$.

	GGA-PBE	GGA-PBEsol
w-SOC	2.2	1.3
w-SOC-vdW	−1.3	−4.3

Our key experimental results are presented in Figs. 2 and 3. We see a clear RS and find a surprising C_2 symmetry rather than C_4 symmetry in the ab plane. Given the fact that we observed additional peaks at half L positions of $(1, 1, L)$ in the x-ray data, we performed the ARPES measurement to understand the origin of these additional peaks. The Fermi surface (FS) and band dispersion along key directions in the BZ for $PtPb_4$ are shown in Figs. 2(a)–2(c). Figure 2(a) shows the ARPES intensity integrated within 10 meV about the chemical potential, which roughly visualizes the FS. The FS consists of at least one electron pocket at the center of the BZ and is surrounded by several other electron pockets. Previous results [51] showed that the crystal structure of $PtPb_4$ has AA stacking of $PtPb_4$ slabs along the tetragonal c axis with space group $P4/nbm$. However, our x-ray and ARPES data point to the possibility of a slight distortion of the crystal structure due to observed C_2 symmetry of the Fermi surface. Figures 2(d)–2(f) show the calculated FS and band dispersion based on the oS20 structure with AB stacking of $PtPb_4$ slabs (with A and B being shifted in the basal plane with respect to each other) with the lattice constant doubled in the c direction. In the calculation, we used the $PtSn_4$ structure with twofold symmetry because it has been shown to be energetically close to the $PtPb_4$ structure. Results seem to be in good agreement with the ARPES data. The measured FS shows significant differences between the x and y directions, and pockets around the X and Y points clearly have different shapes. Despite the tetragonal crystal structure of $PtPb_4$, the ARPES and x-ray scattering data indicate that the band structure at the surface may have different electronic properties than in the bulk. In order to understand this discrepancy between expectations based on the bulk crystal structure and ARPES measurements, we performed extensive band structure calculations.

Given that we see some evidence for twofold symmetry in our ARPES data, we used DFT calculations to determine how energetically removed the possibility of tetragonal structure in $PtPb_4$. To be more specific, Table I shows the energy difference of $E_{tet}-E_{ort}$ between tetragonal and orthorhombic $PtPb_4$ phases without the inclusion of the vdW interactions. It shows that the orthorhombic phase is more stable by −2.2 meV/atom. We also performed a calculation using revised GGA Perdew-Burke-Ernzerhof revised for solids (PBEsol) [52] to verify the calculated relative stability and found that the orthorhombic phase is also more stable within this approximation. We note that both tetragonal and orthorhombic phases are layered structures with a gap of ~3.1 Å between Pb-terminated layers. Therefore, the vdW interactions would play an important role in determining the stability of different phases in this material. With the vdW interactions taken into account, it turns out that the tetragonal phase becomes more stable than the orthorhombic phase by

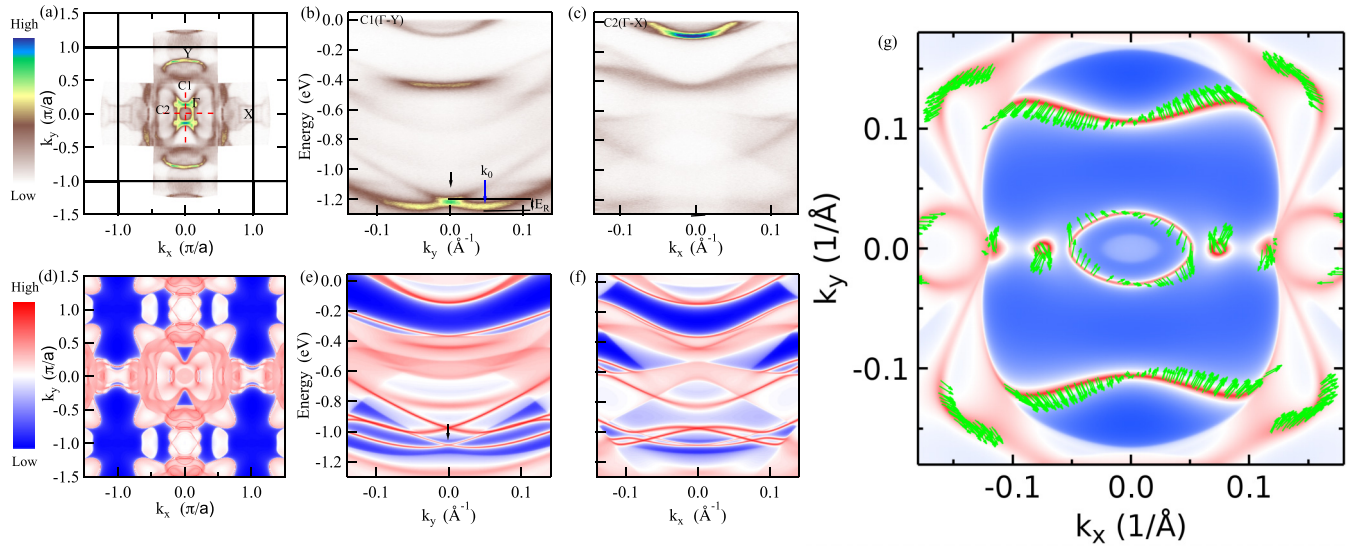

FIG. 2. FS, band dispersion of $PtPb_4$ at 40 K, and calculated FS and band dispersion based on the oS20 $PtSn_4$-type structure. (a) FS plot of the ARPES intensity integrated within 10 meV of the chemical potential along Γ-X and Γ-Y. In this image plot, the brighter color represents higher intensity, and the dark areas represent lower intensities. (b) Band dispersion along the Γ-Y direction; the center of RS is marked by a black arrow. (c) Band dispersion along Γ-X. (d) Calculated FS, (e) calculated band dispersion along Γ-Y, and (f) calculated band dispersion along Γ-X. (g) Isoenergy cut 1.05 eV below E_F with spin texture. Green arrows represent spin orientations on the $k_\parallel$ plane.

−1.3 and −4.3 meV/atom for PBE and PBEsol GGA calculations. However, the energy differences, with and without vdW interaction correction, are very small, on the order of a few kelvins, in terms of thermal energy. In addition, the surface formation energies of these two phases are also very similar, which are 27.23 and 27.95 meV/Å^2 for orthorhombic and tetragonal phases, respectively. The orthorhombic phase has a slightly lower surface formation energy. Therefore, it is very likely that $PtPb_4$ is polymorphic and orthorhombic $PtPb_4$ can be stabilized close to the surface. Based on the x-ray data, DFT calculations, and the ARPES measurement, the actual surface may contain a mixture of domains with different terminations.

In Fig. 3, we focus on the FS and band dispersion in the proximity of the X and Y points. We closely sort out surface and bulk band around the X and Y points from DFT calculations. Figure 4 shows band dispersion around the X and Y points without bulk projection. An enlarged image from the red boxes in Fig. 3(b) is shown in Figs. 3(a) and 3(c). Close to the X point, the FS has two parallel sections that consist of two merged holelike bands, as shown in Figs. 3(c) and 3(j)–3(l). Both bands are quite sharp and intense, which is consistent with a surface origin. The measured band dispersion in this part of the zone agrees quite well with the DFT calculations shown in Figs. 3(m)–3(o). The parallel FS due to surface bands bears some resemblance to $PtSn_4$ and $PdSn_4$ [16,18], although no topological features below E_F are observed here; $PtSn_4$ has Dirac node arc surface states, but $PtPb_4$ shows a linearlike dispersion close to the X point.

The band structure near the Y point is shown in Figs. 3(b) and 3(d)–3(f), while Figs. 3(g)–3(i) show DFT calculations in the same part of the BZ. The ARPES intensity in this part of the BZ is weaker, and bands are much broader, pointing to mostly a bulk origin that causes broadening due to the projection along k_z. The bands with strong surface components predicted by calculations in Figs. 3(h) and 3(i) are not clearly seen, which may indicate that matrix elements likely play a role in suppressing the signal.

We found a clear RS of the valence band. It depicts spin degeneracy lifting at surfaces or interfaces, where inversion symmetry is broken with spin-orbit interaction, which may lead to an asymmetric charge distribution. The relation between the breaking of spin degeneracy and the inversion symmetry can be described by the relativistic effect of moving electrons in a two-dimensional momentum space. The interaction between electron spin and effective magnetic field, originating from a surface electrostatic field, leads to Rashba splitting. As a consequence, the degeneracy is lifted, and the chiral spin texture in the band dispersion and maxima of the valence band or minima of the conduction band are shifted from the symmetry point. Despite the reasonable success of the initially proposed effective model [25,53], this model shows several limitations as well. The most important issue is the magnitude of the splitting. A result based on the effective model shows that the magnitude of splitting is at least several orders of magnitude smaller than that of previously observed data. On top of that, the effective model cannot explain the fact that SOC is stronger in high-Z elements because the strength of electric fields from the surfaces is roughly on the same order of magnitude. Recently, there were several attempts to explain this phenomenon by using numerical and analytic methods [54,55]. Those results point out that RS may be related to the combination of an orbital angular momentum state and electron momentum that introduces asymmetric charge distribution. Although spin-orbit interaction occurs very often in various materials in either bulk or surface states, it is more pronounced in systems with high-Z elements due to the relatively large spin-orbit parameter.

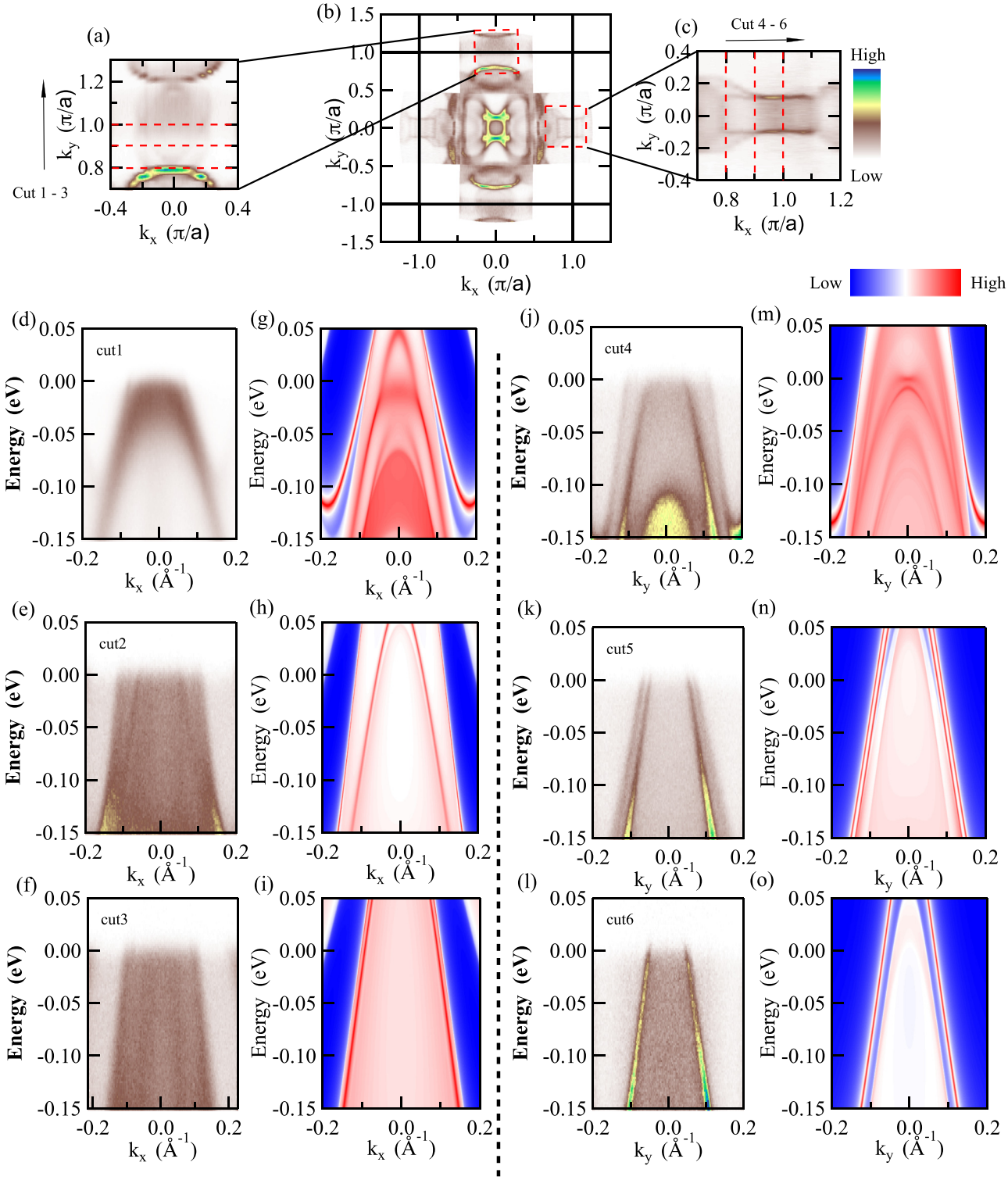

FIG. 3. FS and band dispersion around the X and Y points at 40 K. (a) and (c) Magnified FS around the X and Y points. (b) FS surface of $PtPb_4$ at 40 K. (d)–(f) Band dispersion around the Y point. (g)–(i) DFT calculations corresponding to energy dispersion. (j)–(l) Band dispersion around the X point and (m)–(o) calculated band dispersion corresponding to (j)–(l), respectively.

In some materials, it is not easy to distinguish between Rashba and Dresselhaus splitting experimentally. In order to understand the origin of the band splitting, we performed DFT calculations. Based on the calculation results, we verify that the band splitting occurs at the surface state. The black arrow in Fig. 2(b) shows the position of the RS in the ARPES data. We carefully check the band dispersion from the surface and bulk origin. Figure 5 shows the band dispersion around the Γ point without bulk projection of DFT calculations. It clearly shows the RS with a valence band minimum (VBM)

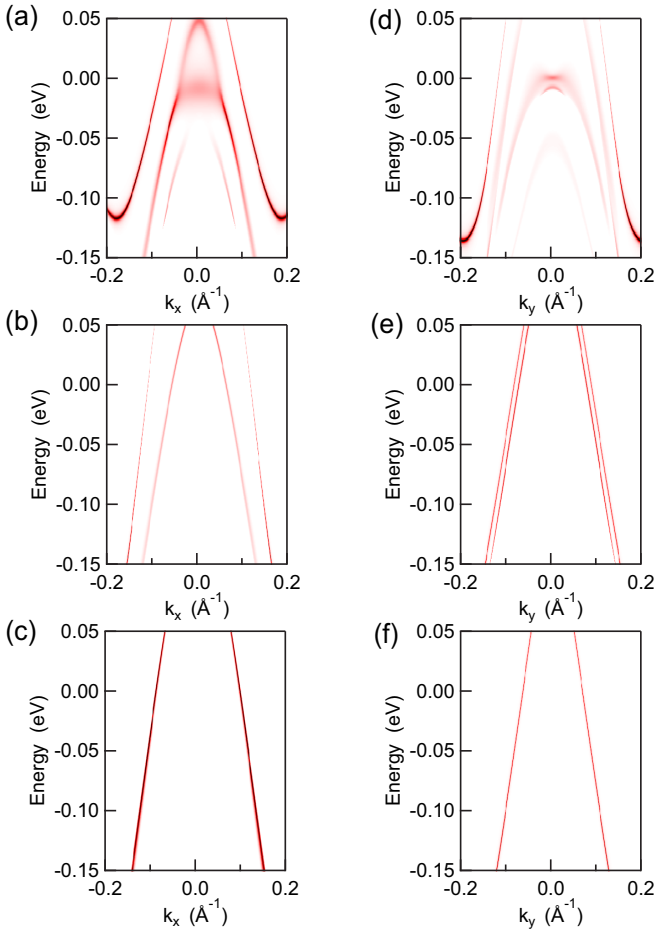

FIG. 4. DFT calculations around zone boundaries. (a)–(c) Band dispersion around the Y point without the bulk projection. (d)–(f) Band dispersion without bulk projection around the X point.

of $E_{\mathrm{VEM}} = 1.3\,\mathrm{eV}$ at the momentum offsets of $\pm k_0$, with $k_0 = 0.04\ \mathrm{Å}^{-1}$, around the Γ. This result shows that the RS in this material is several times bigger than that of Au(111) [27], which is the initially reported ARPES measurement of

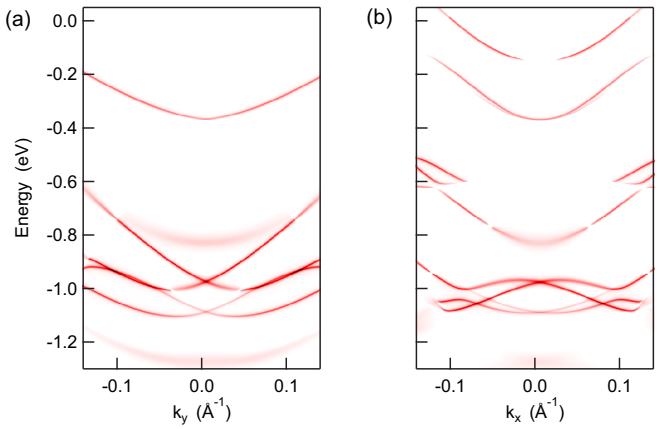

FIG. 5. DFT calculations around the Γ point. (a) Band dispersion along the Γ-Y direction without bulk projection. (b) Band dispersion along the Γ-X direction without bulk projection.

RS. In our ARPES data, the VBM is slightly lower than predicted by calculation. The other important parameter that represents the strength of the RS besides the momentum offset k_0 is the Rashba coupling constant ($\alpha_R = \frac{2E_R}{k_0}$). Using the momentum offset $k_0 \sim 0.045\,\mathrm{Å}^{-1}$ and $E_R \sim 0.04\,\mathrm{eV}$ along the Γ-Y direction, we obtain $\alpha_R \sim 1.7\,\mathrm{eV\,Å}$. This value is on the same order of magnitude of RS in BiTeI, which has one of the largest RSs among previous results [34,35]. Figure 2(c) shows the band dispersion along the Γ-X direction. We find at least one electron pocket in this direction. Figures 2(e) and 2(f) show DFT calculations of the Γ-Y and Γ-X cuts and bear resemblance to the ARPES data modulo a small shift in the energy, which is quite typical. It has been suggested that the forming of RS has something to do with local orbital angular momentum (OAM). Several different theoretical and experimental investigations of the exact role of OAM in RS have been proposed. In a recent paper Park *et al.* [54] offered a theoretical study of RS in a system consisting of p orbitals. In their model, RS is proportional to $\vec{L}\times\vec{k}$, where k is a wave vector of the electron. On the other hand, a mixture of different orbitals was highlighted in Ünzelmann *et al.* [56]. Mixing of different orbitals in surface states introduces OAM and RS proportional to the OAM. Although previous research [54,56] emphasized that mixing of different orbitals plays a major role in the formation of RS, our calculation results show that the RS shows a complex mixture of p_x and p_y orbitals and this system is not suitable for understanding the previous model. The correlation between OAM and RS in this material needs to be scrutinized in future studies.

The outstanding issue is the difference between the observed twofold symmetry of the band structure and the fourfold symmetry of the crystal structure of $PtPb_4$. Our DFT calculations and x-ray data led us to conclude that the symmetry breaking may be caused by an ABAB stacking sequence; the orthorhombic structure is more favorable. Last, we observed RS at the center of the BZ which typically appears at the surface or interface of materials. Even though this effect occurs below E_F, it may be possible by either chemical substitution or gating to move the chemical potential down to utilize this effect in the generation of spin currents at room temperature. This may have interesting consequences not only due to its fundamental importance but also because of its possibility for application to spintronic devices.

ACKNOWLEDGMENTS

This work was supported by the U.S. Department of Energy, Office of Science, Basic Energy Sciences, Materials Science and Engineering Division. Ames Laboratory is operated for the U.S. Department of Energy by Iowa State University under Contract No. DE-AC02-07CH11358. K.L. was supported by CEM, an NSF MRSEC, under Grant No. DMR-1420451. This research used resources of the Advanced Photon Source, a U.S. Department of Energy (DOE) Office of Science User Facility operated for the DOE Office of Science by Argonne National Laboratory under Contract No. DE-AC02-06CH11357.

[1] C. Kane and J. Moore, Topological insulators, Phys. World **24**, 32 (2011).

[2] M. Z. Hasan and C. L. Kane, Colloquium: Topological insulators, Rev. Mod. Phys. **82**, 3045 (2010).

[3] X.-L. Qi and S.-C. Zhang, The quantum spin Hall effect and topological insulators, Phys. Today **63**, 33 (2010).

[4] S.-Y. Xu, I. Belopolski, N. Alidoust, M. Neupane, G. Bian, C. Zhang, R. Sankar, G. Chang, Z. Yuan, C.-C. Lee *et al.*, Discovery of a Weyl fermion semimetal and topological Fermi arcs, Science **349**, 613 (2015).

[5] J. E. Moore, The birth of topological insulators, Nature (London) **464**, 194 (2010).

[6] G. Li, C. Fu, W. Shi, L. Jiao, J. Wu, Q. Yang, R. Saha, M. E. Kamminga, A. K. Srivastava, E. Liu *et al.*, Dirac nodal arc semimetal $PtSn_4$: An ideal platform for understanding surface properties and catalysis, Angew. Chem. (2019).

[7] S. Belyakov and C. Gourlay, Heterogeneous nucleation of β-Sn on $NiSn_4$, $PdSn_4$ and $PtSn_4$, Acta Mater. **71**, 56 (2014).

[8] J. F. Kuhmann, C.-H. Chiang, P. Harde, F. Reier, W. Österle, I. Urban, and A. Klein, Pt thin-film metallization for FC-bonding using SnPb60/40 solder bump metallurgy, Mater. Sci. Eng. A **242**, 22 (1998).

[9] B. Kempf and S. Schmauder, Thermodynamic modeling of precious metals alloys, Gold Bull. **31**, 51 (1998).

[10] B. T. Biggs, S. Taylor, and E. Van der Lingen, The hardening of platinum alloys for potential jewellery application, Platinum Met. Rev. **49**, 2 (2005).

[11] Y. Wang, D. Zhu, Y. Wu, Y. Yang, J. Yu, R. Ramaswamy, R. Mishra, S. Shi, M. Elyasi, K.-L. Teo, Y. Wu, and H. Yang, Room temperature magnetization switching in topological insulator-ferromagnet heterostructures by spin-orbit torques, Nat. Commun. **8**, 1364 (2017).

[12] B. Ghosh, S. Mardanya, B. Singh, X. Zhou, B. Wang, T.-R. Chang, C. Su, H. Lin, A. Agarwal, and A. Bansil, Saddle-point Van Hove singularity and dual topological state in Pt_2HgSe_3, Phys. Rev. B **100**, 235101 (2019).

[13] S.-Y. Xu *et al.*, Experimental discovery of a topological Weyl semimetal state in TaP, Sci. Adv. **1**, e1501092 (2015).

[14] I. Cucchi, A. Marrazzo, E. Cappelli, S. Riccò, F. Y. Bruno, S. Lisi, M. Hoesch, T. K. Kim, C. Cacho, C. Besnard, E. Giannini, N. Marzari, M. Gibertini, F. Baumberger, and A. Tamai, Bulk and Surface Electronic Structure of the Dual-Topology Semimetal Pt_2HgSe_3, Phys. Rev. Lett. **124**, 106402 (2020).

[15] S.-M. Huang, S.-Y. Xu, I. Belopolski, C.-C. Lee, G. Chang, B. Wang, N. Alidoust, G. Bian, M. Neupane, C. Zhang, S. Jia, A. Bansil, H. Lin, and Z. Hasan, A Weyl Fermion semimetal with surface Fermi arcs in the transition metal monopnictide TaAs class, Nat. Commun. **6**, 7373 (2015).

[16] Y. Wu, L.-L. Wang, E. Mun, D. D. Johnson, D. Mou, L. Huang, Y. Lee, S. L. Bud'ko, P. C. Canfield, and A. Kaminski, Dirac node arcs in $PtSn_4$, Nat. Phys. **12**, 667 (2016).

[17] E. Mun, H. Ko, G. J. Miller, G. D. Samolyuk, S. L. Bud'ko, and P. C. Canfield, Magnetic field effects on transport properties of $PtSn_4$, Phys. Rev. B **85**, 035135 (2012).

[18] N. H. Jo, Y. Wu, L.-L. Wang, P. P. Orth, S. S. Downing, S. Manni, D. Mou, D. D. Johnson, A. Kaminski, S. L. Bud'ko, and P. C. Canfield, Extremely large magnetoresistance and Kohler's rule in $PdSn_4$: A complete study of thermodynamic, transport, and band-structure properties, Phys. Rev. B **96**, 165145 (2017).

[19] M. Gendron and R. Jones, Superconductivity in the $CuAl_2$ (C16) crystal class, J. Phys. Chem. Solids **23**, 405 (1962).

[20] S. Siahrostami, A. Verdaguer-Casadevall, M. Karamad, D. Deiana, P. Malacrida, B. Wickman, M. Escudero-Escribano, E. A. Paoli, R. Frydendal, T. W. Hansen, I. Chorkendor, I. E. L. Stephens, and J. Rossmeisl, Enabling direct H_2O_2 production through rational electrocatalyst design, Nat. Mater. **12**, 1137 (2013).

[21] $PtPb_4$ crystal structure, datasheet from PAULING FILE Multinaries Edition–2012, https://materials.springer.com/isp/crystallographic/docs/sd_1250530.

[22] A. Manchon, H. C. Koo, J. Nitta, S. Frolov, and R. Duine, New perspectives for Rashba spin–orbit coupling, Nat. Mater. **14**, 871 (2015).

[23] H. C. Koo, J. H. Kwon, J. Eom, J. Chang, S. H. Han, and M. Johnson, Control of spin precession in a spin-injected field effect transistor, Science **325**, 1515 (2009).

[24] J. Wunderlich, B.-G. Park, A. C. Irvine, L. P. Zârbo, E. Rozkotová, P. Nemec, V. Novák, J. Sinova, and T. Jungwirth, Spin Hall effect transistor, Science **330**, 1801 (2010).

[25] R. Casella, Toroidal Energy Surfaces in Crystals with Wurtzite Symmetry, Phys. Rev. Lett. **5**, 371 (1960).

[26] E. Rotenberg, J. W. Chung, and S. D. Kevan, Spin-Orbit Coupling Induced Surface Band Splitting in Li/W (110) and Li/Mo (110), Phys. Rev. Lett. **82**, 4066 (1999).

[27] S. LaShell, B. A. McDougall, and E. Jensen, Spin Splitting of an Au (111) Surface State Band Observed with Angle Resolved Photoelectron Spectroscopy, Phys. Rev. Lett. **77**, 3419 (1996).

[28] Y. M. Koroteev, G. Bihlmayer, J. E. Gayone, E. V. Chulkov, S. Blügel, P. M. Echenique, and P. Hofmann, Strong Spin-Orbit Splitting on Bi Surfaces, Phys. Rev. Lett. **93**, 046403 (2004).

[29] C. R. Ast, J. Henk, A. Ernst, L. Moreschini, M. C. Falub, D. Pacilé, P. Bruno, K. Kern, and M. Grioni, Giant Spin Splitting through Surface Alloying, Phys. Rev. Lett. **98**, 186807 (2007).

[30] C. R. Ast, D. Pacilé, L. Moreschini, M. C. Falub, M. Papagno, K. Kern, M. Grioni, J. Henk, A. Ernst, S. Ostanin, and P. Bruno, Spin-orbit split two-dimensional electron gas with tunable Rashba and Fermi energy, Phys. Rev. B **77**, 081407(R) (2008).

[31] E. Frantzeskakis, S. Pons, H. Mirhosseini, J. Henk, C. R. Ast, and M. Grioni, Tunable Spin Gaps in a Quantum-Confined Geometry, Phys. Rev. Lett. **101**, 196805 (2008).

[32] K. He, T. Hirahara, T. Okuda, S. Hasegawa, A. Kakizaki, and I. Matsuda, Spin Polarization of Quantum Well States in Ag Films Induced by the Rashba Effect at the Surface, Phys. Rev. Lett. **101**, 107604 (2008).

[33] S. Hatta, T. Aruga, Y. Ohtsubo, and H. Okuyama, Large Rashba spin splitting of surface resonance bands on semiconductor surface, Phys. Rev. B **80**, 113309 (2009).

[34] H. Maaß, H. Bentmann, C. Seibel, C. Tusche, S. V. Eremeev, T. R. F. Peixoto, O. E. Tereshchenko, K. A. Kokh, E. V. Chulkov, J. Kirschner, and F. Reinert, Spin-texture inversion in the giant Rashba semiconductor BiTeI, Nat. Commun. **7**, 11621 (2016).

[35] K. Ishizaka *et al.*, Giant Rashba-type spin splitting in bulk BiTeI, Nat. Mater. **10**, 521 (2011).

[36] J. R. Bindel, M. Pezzotta, J. Ulrich, M. Liebmann, E. Y. Sherman, and M. Morgenstern, Probing variations of the Rashba spin–orbit coupling at the nanometre scale, Nat. Phys. **12**, 920 (2016).

[37] M. Liebmann *et al.*, Giant Rashba-type spin splitting in ferroelectric GeTe (111), Adv. Mater. **28**, 560 (2016).

[38] H. J. Elmers *et al.*, Spin mapping of surface and bulk Rashba states in ferroelectric α-GeTe (111) films, Phys. Rev. B **94**, 201403(R) (2016).

[39] H. Okamoto, *Phase Diagrams for Binary Alloys: Desk Handbook* (ASM International, Materials Park, OH, 2000).

[40] P. C. Canfield, T. Kong, U. S. Kaluarachchi, and N. H. Jo, Use of frit-disc crucibles for routine and exploratory solution growth of single crystalline samples, Philos. Mag. **96**, 84 (2016).

[41] A. Kreyssig, S. Chang, Y. Janssen, J. W. Kim, S. Nandi, J. Q. Yan, L. Tan, R. J. McQueeney, P. C. Canfield, and A. I. Goldman, Crystallographic phase transition within the magnetically ordered state of Ce_2Fe_{17}, Phys. Rev. B **76**, 054421 (2007).

[42] W. Kohn and L. J. Sham, Self-consistent equations including exchange and correlation effects, Phys. Rev. **140**, A1133 (1965).

[43] G. Kresse and J. Furthmüller, Efficiency of *ab-initio* total energy calculations for metals and semiconductors using a plane-wave basis set, Comput. Mater. Sci. **6**, 15 (1996); Efficient iterative schemes for *ab initio* total-energy calculations using a plane-wave basis set, Phys. Rev. B **54**, 11169 (1996).

[44] P. E. Blöchl, Projector augmented-wave method, Phys. Rev. B **50**, 17953 (1994).

[45] G. Kresse and D. Joubert, From ultrasoft pseudopotentials to the projector augmented-wave method, Phys. Rev. B **59**, 1758 (1999).

[46] J. P. Perdew, K. Burke, and M. Ernzerhof, Generalized Gradient Approximation Made Simple, Phys. Rev. Lett. **77**, 3865 (1996).

[47] H. J. Monkhorst and J. D. Pack, Special points for Brillouin-zone integrations, Phys. Rev. B **13**, 5188 (1976).

[48] S. Grimme, J. Antony, S. Ehrlich, and H. Krieg, A consistent and accurate ab initio parametrization of density functional dispersion correction (DFT-D) for the 94 elements H-Pu, J. Chem. Phys. **132**, 154104 (2010).

[49] S. Grimme, S. Ehrlich, and L. Goerigk, Effect of the damping function in dispersion corrected density functional theory, J. Comput. Chem. **32**, 1456 (2011).

[50] R. Jiang, D. Mou, Y. Wu, L. Huang, C. D. McMillen, J. Kolis, H. G. Giesber, III, J. J. Egan, and A. Kaminski, Tunable vacuum ultraviolet laser based spectrometer for angle resolved photoemission spectroscopy, Rev. Sci. Instrum. **85**, 033902 (2014).

[51] E.-L. Nordmark, O. Wallner, and U. Häussermann, Polymorphism of $IrSn_4$, J. Solid State Chem. **168**, 34 (2002).

[52] J. P. Perdew, A. Ruzsinszky, G. I. Csonka, O. A. Vydrov, G. E. Scuseria, L. A. Constantin, X. Zhou, and K. Burke, Restoring the Density-Gradient Expansion for Exchange in Solids and Surfaces, Phys. Rev. Lett. **100**, 136406 (2008).

[53] Y. A. Bychkov and É. I. Rashba, Properties of a 2D electron gas with lifted spectral degeneracy, JETP Lett. **39**, 78 (1984).

[54] S. R. Park, C. H. Kim, J. Yu, J. H. Han, and C. Kim, Orbital-Angular-Momentum Based Origin of Rashba-Type Surface Band Splitting, Phys. Rev. Lett. **107**, 156803 (2011).

[55] M. Nagano, A. Kodama, T. Shishidou, and T. Oguchi, A first-principles study on the Rashba effect in surface systems, J. Phys.: Condens. Matter **21**, 064239 (2009).

[56] M. Ünzelmann, H. Bentmann, P. Eck, T. Kißlinger, B. Geldiyev, J. Rieger, S. Moser, R. C. Vidal, K. Kißner, L. Hammer, M. Alexander Schneider, T. Fauster, G. Sangiovanni, D. Di Sante, and F. Reinert, Orbital-Driven Rashba Effect in a Binary Honeycomb Monolayer AgTe, Phys. Rev. Lett. **124**, 176401 (2020).